Review of Scientific Instruments

RESEARCH ARTICLE | JULY 22 2024

Simulation of a scintillator-based fast ion loss detector for steady-state operation in Wendelstein 7-X (invited) FREE

Special Collection: Proceedings of the 25th Topical Conference on High-Temperature Plasma Diagnostics

A. LeViness ; S. A. Lazerson ; A. Jansen van Vuuren ; J. Rueda-Rueda ; J. Ayllon-Guerola ; S. Bozhenkov ; D. Corl ; R. Ellis ; J. Galdon-Quiroga ; J. Garcia-Dominguez ; M. Garcia-Munoz ; J. Hidalgo-Salaverri ; K. Ogawa ; N. Pablant ; J. Segado-Fernandez ; W7-X Team

Rev. Sci. Instrum. 95, 073529 (2024)
https://doi.org/10.1063/5.0214788

Review of Scientific Instruments ARTICLE pubs.aip.org/aip/rsi

Simulation of a scintillator-based fast ion loss detector for steady-state operation in Wendelstein 7-X (invited)

Cite as: Rev. Sci. Instrum. 95, 073529 (2024); doi: 10.1063/5.0214788
Submitted: 19 April 2024 • Accepted: 1 July 2024 •
Published Online: 22 July 2024

A. LeViness,[1,a] S. A. Lazerson,[2,b] A. Jansen van Vuuren,[3] J. Rueda-Rueda,[4] J. Ayllon-Guerola,[4] S. Bozhenkov,[2] D. Corl,[1] R. Ellis,[1] J. Galdon-Quiroga,[4] J. Garcia-Dominguez,[1] M. Garcia-Munoz,[4] J. Hidalgo-Salaverri,[4] K. Ogawa,[5] N. Pablant,[1] J. Segado-Fernandez,[4] and W7-X Team[c]

AFFILIATIONS

[1] Princeton Plasma Physics Laboratory, Princeton, New Jersey 08540, USA
[2] Max Planck Institute for Plasma Physics, Greifswald 17491, Germany
[3] Swiss Federal Institute of Technology Lausanne, Lausanne 1015, Switzerland
[4] University of Seville, Seville 41004, Spain
[5] National Institute for Fusion Science, Toki 509-5202, Japan

Note: This paper is part of the Special Topic on Proceedings of the 25th Topical Conference on High-Temperature Plasma Diagnostics.

[a] **Author to whom correspondence should be addressed:** leviness@pppl.gov
[b] **Present address:** Gauss Fusion GmbH, Garching 85748, Germany.

[c] See Thomas Sunn Pedersen *et al.*, Nucl. Fusion **62**, 042022 (2022) for the full list of W7-X team members.

ABSTRACT

A quantitative theoretical framework has been created to model neutral beam injection and fast ion losses in the Wendelstein 7-X (W7-X) stellarator, including a novel method to develop synthetic diagnostics for fast ion loss detectors (FILDs) of many types, such as scintillating and Faraday Cup FILDs. This is the first time that this has been done in stellarator geometry with this level of fidelity, providing a way for fast ion losses to be predicted more precisely in future stellarator experiments and in W7-X. Simulations of the signal seen by a Faraday Cup FILD have been completed for multiple W7-X plasmas and show close agreement with the measured signals. This method is now applied to an actively water-cooled, scintillator-based FILD, which is currently in development to measure the fast ion loss distribution in W7-X in greater detail. The design makes use of a double slit to measure energy-and-pitch-angle-resolved losses of both co-going and counter-going fast ions. The diagnostic, which can be inserted to different radial positions, has been designed to withstand steady-state heat fluxes of up to 120 kW/m^2 along with additional transient heat loads of 100 kW/m^2 lasting for up to 20 s at a time. Simulations of W7-X standard magnetic configuration show up to 8×10^{13} (s^{-1} cm^{-2}) ion fluxes onto the sensor from each neutral beam source and no signal from the counter-going slit. These simulations will help inform experimental proposals for future W7-X campaigns after installation of this diagnostic.

I. INTRODUCTION

The confinement of fast ions, such as those produced by fusion reactions or by plasma heating methods such as neutral beam injection (NBI) or ion cyclotron resonance heating (ICRH), is crucial to the efficient operation of a plasma device or fusion reactor as well as to the protection of vessel walls and other plasma facing components. The question of fast ion confinement is especially important for stellarators, which do not inherently confine trapped particle orbits in the way that axisymmetric devices do and which must, therefore, be optimized to better confine these fast ions.[1]

The Wendelstein 7-X (W7-X) stellarator was numerically optimized for good fast ion confinement as an important aspect of its design.[2] For this reason, confirming this good confinement is a key scientific goal of W7-X. Measurements of lost fast ions can be made with diagnostics such as fast ion loss detectors (FILDs), which come in several different types.

The two most popular FILD types are the scintillator type and the Faraday Cup type.[3–8] The former is composed of a phosphorescent screen onto which charged particles impinge, releasing photons, which are then measured by a video camera and/or an array of photomultiplier tubes. The second is composed of thin metal films that measure the flux of arriving ions as a current. Faraday Cup FILDs tend to have higher time resolution, while scintillator FILDs have higher spatial resolution, particularly when paired with a video camera. Through the use of a pinhole and collimating structure, fast ions arriving at the FILD can be spread out based on their gyroradius (and thus energy) and pitch angle, meaning that spatial resolution at the scintillator corresponds to resolution in energy and pitch angle.

There are three FILDs either implemented on or planned for W7-X. The two which have already been used on W7-X, referred to in this work as the NIFS-FILD and the FC-FILD, are both Faraday Cup types. The NIFS-FILD, provided by the National Institute for Fusion Science in Japan, has been mounted on the multi-purpose manipulator (MPM)[9] for experiments during the first two experimental campaigns on W7-X making use of NBI. It makes use of a pinhole and collimating structure, along with an array of eight sensors, to measure energy-and-pitch-resolved losses of fast ions.[10] The FC-FILD, implemented as a permanent diagnostic in the second NBI campaign, makes use of five sensors with varying thicknesses of insulation in order to resolve fast ion losses in energy, without any resolution in pitch angle.[11–13]

This work focuses on the development of a third FILD for W7-X, referred to in this work as the S-FILD, which consists of a scintillator material layered over a Faraday Cup and paired with a video camera, which can thus measure losses with high resolution in energy and pitch angle, and measure the total arriving ion flux with high time resolution.[14,15] This method of placing a Faraday Cup underneath a scintillator layer for measurement of total flux has been used in many FILDs, including on CHS,[4] W7-AS,[5,16] NSTX,[17] ASDEX-U,[6] and K-STAR.[18] The S-FILD was designed with two separate pinholes for the measurement of both co-and-counter-going ions and will be located directly next to the FC-FILD, allowing the two diagnostics to take complementary measurements. The S-FILD would be the first scintillating-type FILD on W7-X and would take measurements with much higher resolution in energy and pitch angle than either of the currently existing FILDs are capable of.

As W7-X has recently begun long-pulse operation, with plasmas lasting for more than eight minutes, with more than 1 GJ of injected energy achieved and 18 GJ injected energy planned, it was necessary to design the S-FILD with active water-cooling to withstand heat fluxes of up to 120 kW/m^2 in steady-state operation, with an additional 100 kW/m^2 for up to 20 s at a time (see Ref. 15). The S-FILD will be mounted on a reciprocating structure so that it can be inserted in and out of the vessel to minimize transient heat loads.

This paper will first describe the completed design of the S-FILD, with a focus on the physics aspects. Following this, simulations of fast ion losses in the standard magnetic configuration of W7-X are presented, making use of the simulation method first outlined in Ref. 19, including a synthetic signal to the Faraday Cup of fast ion flux over time and the spatial pattern of fast ion strikes on the scintillator plate.

II. DESIGN OF THE S-FILD SYSTEM

A. Probe head

The S-FILD probe head will consist of a 3D-printed stainless steel structure covered with graphite tiles for thermal protection, as shown in Fig. 1. The front face of the probe head has been designed to be parallel to the last closed flux surface (LCFS) of the standard W7-X magnetic configuration when the probe head is fully inserted into the vessel. There are two pinholes, one on either side of the probe head, which allow for co-and-counter-going fast ions to enter, where, based on their energies and pitch angles, they will either land on the scintillator plate or be absorbed by the collimating slits inside of the probe head.

Inside the probe head, parallel to the front face of the structure and thus to the LCFS, will be a stainless steel plate onto which will be deposited a layer of $SrGa_2S_4:Eu^{2+}$ (TG-Green), a phosphorescent material that releases light when impacted by charged particles. This light can then be measured by using a fast video camera outside the vessel. The layout of this plate within the probe head is shown in Fig. 2, with the two collimating slits shown in red, and a simplified cutaway view of the geometry of the counter-going side, showing the pinhole and collimating slit in relation to the scintillator, is shown in Fig. 3.

The stainless steel plate, which is electrically isolated from the rest of the probe head, also doubles as a Faraday Cup, measuring the

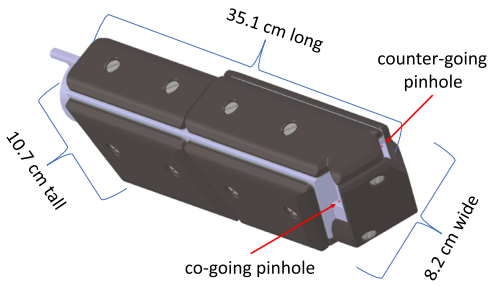

FIG. 1. Probe head of the S-FILD diagnostic, composed of a stainless steel 3D-printed piece covered with graphite tiles for thermal protection. The pinholes are shown in red. The dimensions shown include the graphite protection tiles, and the length is given from the end of the graphite tiles to the furthest point on the front face.

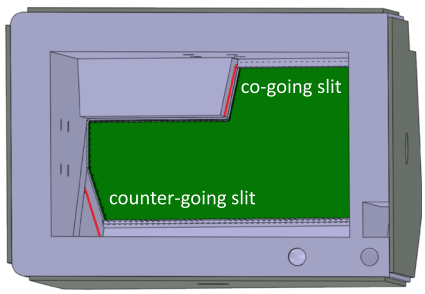

FIG. 2. Position of the scintillator (green) within the probe head, with the collimating slits shown in red. The scintillator is inside and parallel to the front face of the probe head. The graphite tiles are not shown.

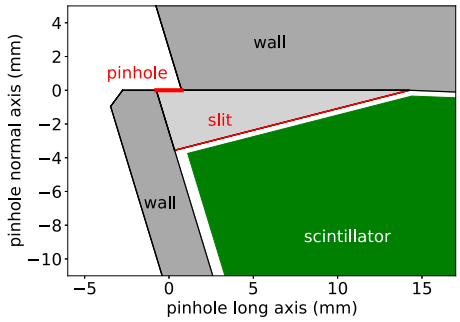

FIG. 3. Cutaway view of a simplified geometry of the probe head, showing the counter-going pinhole and collimating slit along with the corner of the scintillator.

flux of fast ions to the screen as a current. Underneath this plate is a layer of insulating material and a second Faraday Cup, this one meant to measure any noise, such as that produced by coupling to the plasma so that it can be removed from the signal, a method that has previously been employed on FILDs in ASDEX-U.[6] The signal to the Faraday Cup has no spatial resolution but is expected to have a higher time resolution than the scintillator signal. The maximum speed of the CMOS camera planned for use in this diagnostic (the C-Blue One 1608 × 1104 pix with 9 μm/pix camera from First Light Imaging) at full frame with 12 bits is 481 fps (Hz), while the sampling rate of the Faraday Cup signal is limited only by the choice of digitizer.

The spatial resolution of the camera signal is important because, due to the collimating structure, the location of the light on the scintillator plate gives information about the gyroradii (and thus energies) and pitch angles of the fast ions arriving at the plate. Figure 4 shows the strike maps of the average strike location, for a given pitch angle $[\cos^{-1}\left(\frac{v_\parallel}{v}\right)$, given in units of degrees] and "gyroscalar,"[20] a quantity related to the gyroradius ($\frac{mv}{|q|B} = \frac{v}{v_\perp} r_{gyro}$, where r_{gyro} is the gyroradius, given in units of cm), of markers arriving onto the sensor from each of the two pinholes. It should be noted that while the W7-X NBI system can only produce ions with gyroscalars up to 1.5 cm, the S-FILD is capable of measuring those with higher values and thus higher energies. This may be important in future campaigns, which, by making use of combined NBI-ICRH heating, may produce fast ions with energies greater than those produced by the W7-X NBI system alone.

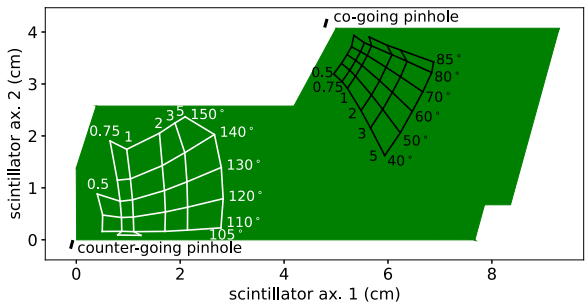

FIG. 4. Strike maps showing the average strike location on the scintillator for co- and-counter-going fast ions. Each point corresponds to a pitch angle, gyroscalar pair. These were produced using the FILDSIM code[21] and excluding from consideration any markers that were shadowed by the exterior of the probe head when moving backward in time from the pinholes.

B. Manipulator arm

The S-FILD probe head, such as the FC-FILD, will be mounted on a reciprocating arm and inserted into the port AEN21, in the same W7-X module as the neutral beam ports. The FC-FILD is located on the central flange in this port, while the S-FILD will be located on the flange directly below it. The manipulator arm, controlled by a pneumatic motion drive system, will be able to insert the S-FILD from a parked position flush with the vacuum vessel wall up to a fully inserted position of about 26 cm toward the plasma from the parked position. The position of the probe head with respect to the plasma can be chosen by changing the position of a hard stop plate controlled by a stepper motor between plasma shots.

The manipulator arm, in addition to allowing for insertion of the probe head, will also contain an optical system consisting of a series of lenses, mirrors, and vacuum windows to relay the light produced by the scintillator to the CMOS camera mounted outside the vacuum vessel, mounted on a sliding rail to keep a fixed optical distance between the camera and scintillator plate as the probe head is inserted. It will also contain tubes for active water cooling of the probe head and arm to avoid overheating of the diagnostic; a thermocouple for measuring the temperature of the probe head; co-axial cables carrying the signal from the Faraday Cup; and a fiber optic cable for illumination of the scintillator plate so that the camera image can be spatially calibrated.

The steady-state nature of the W7-X device makes cooling, and careful measurement of the probe head temperature, a necessity. The scintillator material, TG-Green, shows inhibited response even at temperatures of 200 °C, with very little signal once temperatures reach 400 °C or above.[22] In addition, it must be guaranteed that the temperature rise will not cause structural damage to the probe head and manipulator arm. For thermal analysis, it was assumed that the steel probe head will absorb up to 20 kW/m^2 of stray ECRH radiation and that the heat flux from exposure to the plasma will be around 100 kW/m^2, with an additional 100 kW/m^2 of fast ion heat loads when the NBI is in operation, for up to 20 s at a time, meaning that the diagnostic must withstand stationary heat loads of 120 kW/m^2 and transient heat loads of 220 kW/m^2.

A detailed thermomechanical analysis of the diagnostic can be found in Ref. 15. It is found that in the steady-state case with the most conservative estimates of heat flux, the graphite tiles reach a maximum temperature of 775 °C, and in the case of transient NBI loads, 985 °C, both far less than the sublimation temperature of graphite. The temperature reached by the stainless steel structure is even less than that, and the interior face of the probe head, on which the scintillator plate rests, reaches a maximum of 245 °C in the transient (highest heat load) case, which is still within the operating limits for the TG-Green material. While the scintillator response would be inhibited at this temperature, the signal would still be measurable and the scintillator would not be damaged. This transient case is a worst-case scenario, which would require four NBI sources to be operated back-to-back for 5 s each, something that has not yet been performed on W7-X and is not planned. Even

in this scenario, the temperature rise of the probe head is not predicted to lead to untenable physical stresses on the structure.[15] In addition, much of the design of the S-FILD diagnostic was based on that of the neighboring FC-FILD, which never exceeded 100° measured by its thermocouple within normal operation[13] and only reached temperatures of around 180° in one unusual magnetic field configuration.

III. METHOD FOR SIMULATING S-FILD SIGNAL

Simulation of signal to the FILD is performed using a method similar to that first outlined in Ref. 19, which was used to simulate a Faraday Cup type FILD, the NIFS-FILD, previously used in experiments in W7-X,[10] finding the first quantitative agreement between the simulation and measurement of fast ion losses on W7-X.[19] The method aims to compensate for the large difference in scale between the last closed flux surface (LCFS) of the plasma and the entrance pinholes to the FILD by making use of multiple expansions around the ion guiding centers and intermediate virtual detection planes. For this work, the method, which was developed to calculate the total fast ion flux to a Faraday plate, has been extended to include spatial information at the plate, allowing for the determination of a spatially resolved signal for comparison with the camera image of the scintillator.

First, the equilibrium solver code VMEC (in free-boundary mode) and neoclassical code NEOTRANSP,[23] which, in turn, uses the DKES (drift kinetic equation solver) code,[24] are used to find a self-consistent magnetic equilibrium based on the coil currents for the standard magnetic configuration of W7-X and prescribed density and temperature profiles. Following this, the validated deposition model[25] of the Monte Carlo orbit following the BEAMS3D[26] code is used to simulate injection of the four neutral beams already commissioned for use in W7-X.[27,28] "Markers" representing fast ions produced by the NBI are then followed using the drift kinetic equations,

$$\frac{d\vec{R}}{dt} = \frac{\hat{b}}{qB} \times \left(\mu \nabla B + \frac{m v_\parallel^2}{B} (\hat{b} \cdot \nabla) \vec{B} \right) + v_\parallel \hat{b} + \frac{\vec{E} \times \vec{B}}{B^2}, \tag{1}$$

$$\frac{dv_\parallel}{dt} = -\frac{\mu}{m} \hat{b} \cdot (\nabla B), \tag{2}$$

where $\vec{R}$ is the ion's guiding center position, $\hat{b} = \frac{\vec{B}}{B}$ is the direction of the magnetic field, $\mu = \frac{1}{2} \frac{m v_\perp^2}{B}$ is the magnetic moment, $v_\parallel = \frac{d\vec{R}}{dt} \cdot \hat{b}(\vec{R})$ is the component of the velocity parallel to the magnetic field, and $\vec{E} = -\nabla \Phi$ is the electric field, which is assumed to only point perpendicular to $\hat{b}$.[26] The effects of collisions and pitch angle scattering are included between integration time steps.[29] The markers representing fast ions are followed until they thermalize or reach the last closed flux surface (LCFS) as defined by the VMEC equilibrium, at which point they are considered lost.

The lost markers are used as input for the Monte Carlo orbit-following code ASCOT5[30] in a workflow similar to that described in Refs. 19 and 31. These lost markers are multiplied to create 60 new markers for each one lost through the LCFS. Each new marker has the same guiding center location and energy as the original one but is given a random gyrophase and a random perturbation between −1% and 1% to the pitch (defined as $\frac{v_\parallel}{v}$). These new markers are followed using ASCOT5 in full-orbit mode without collisions or radial electric field until they hit the wall, defined from a 3D triangular mesh created from CAD models of the W7-X vacuum vessel, ports, and the S-FILD diagnostic at full insertion.

Using the "Poincaré" function of ASCOT5, two transparent planes at two constant values of the toroidal angle ϕ are set up such that all ions reaching each of the two pinholes will have to pass through them, and the information for each marker is saved as it passes through the plane. These markers are sorted into bins in the spatial coordinates, R and Z, along with pitch angle, gyroscalar, and gyrophase, defined here as

$$\chi = \cos^{-1}\left(\frac{v_\parallel}{v} \right), \tag{3}$$

$$\rho_L = \frac{mv}{|q|B} = \frac{v}{v_\perp} r_{gyro}, \tag{4}$$

$$\zeta = \tan^{-1}\left(\frac{-\hat{v}_\perp \cdot (\hat{b} \times \hat{z})}{\hat{v}_\perp \cdot \hat{z}} \right), \tag{5}$$

where m is the mass, $|q|$ is the absolute value of the particle's charge, B is the magnitude of the magnetic field strength $|\vec{B}|$, $\hat{b}$ is the direction of the magnetic field $\frac{\vec{B}}{B}$, v is the magnitude of the total marker velocity $|\vec{v}|$, $v_\parallel$ is the parallel velocity $\vec{v} \cdot \hat{b}$, $v_\perp$ is the magnitude of the perpendicular velocity vector $|\vec{v}_\perp| = |\vec{v} - v_\parallel \hat{b}|$, $\hat{v}_\perp$ is the direction of this vector $\frac{\vec{v}_\perp}{v_\perp}$, $\hat{z}$ is the direction of the Z axis, and r_{gyro} is the gyroradius.

For each marker saved at the virtual plane, the guiding center is found and an expansion around it is performed, creating 1000 new markers with the same χ and ρ_L, but with ζ evenly distributed between 0 and 2π and (R, Z) determined accordingly. If any of these 1000 markers is determined to have any probability of making it to the scintillator, all 1000 are then traced backward for 10 gyro-orbits. Those markers that intersect the side of the probe head within this time are removed from consideration, and the weight is redistributed among the remaining markers.

Separate simulations are performed, for each of the two pinholes, following markers, in sets of constant (χ, ρ_L, ζ), backward and forward from the pinhole in full-orbit, collisionless ASCOT5 simulations until they reach the virtual plane (when running backward) or the scintillator plate (when running forward), or else are stopped by intersecting parts of the probe head. As described in Ref. 19, for each (χ, ρ_L, ζ) set, markers are found that have one specified value of gyrophase at the virtual plane, ζ'. Contours of constant ζ' at the planes form straight lines at the planes and in the pinholes, so that only two markers are necessary.

For each combination of $(\chi, \rho_L, \zeta, \zeta')$, the two markers are found that form a line in both the (R, Z) plane and the pinhole. This is repeated for multiple values of ζ at the pinhole, forming a quadrilateral, as shown in Fig. 5. Here, the blue and orange lines within the pinhole and at the plane correspond to markers that begin in the pinhole with (χ, ρ_L, ζ_1) and (χ, ρ_L, ζ_2), respectively, and reach the plane with our desired ζ'. To separate into the (R, Z) bins, the fragment of the (R, Z) grid within this quadrilateral is then mapped into the pinhole based on the relative position of the blue and orange lines.

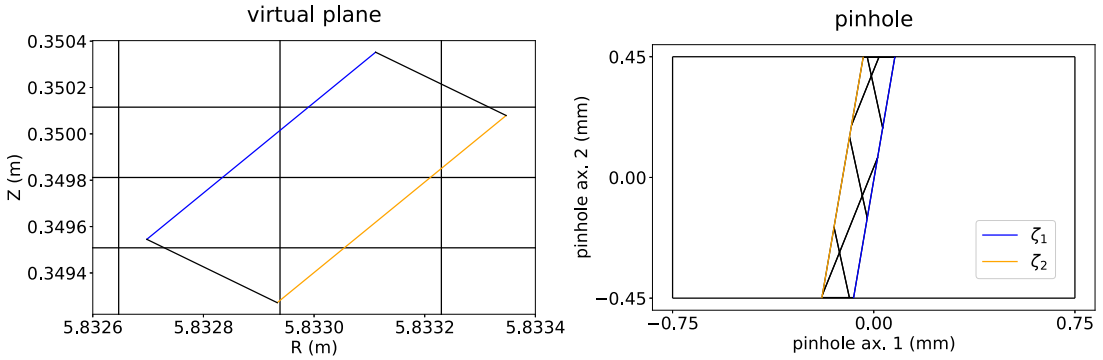

FIG. 5. Position on the virtual plane and within the pinhole for markers that, beginning from the virtual plane with a specific value of (χ, ρ_L, ζ'), arrive at the pinhole with a gyrophase $\zeta \in [\zeta_1, \zeta_2]$. The division of the (R, Z) plane into bins is mapped to the pinhole for this set as well.

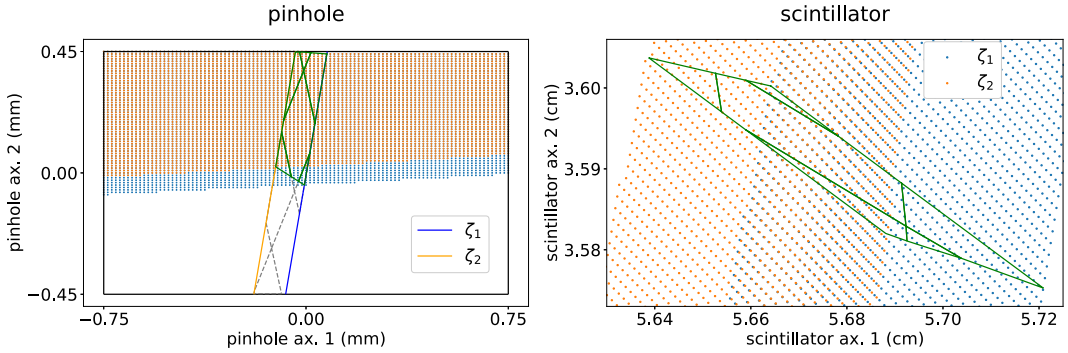

FIG. 6. Overlap between the plane-to-pinhole mapping found in the previous step and the markers that, beginning as an evenly spaced grid within the pinhole with (χ, ρ_L, ζ_1) and (χ, ρ_L, ζ_2), pass through to the scintillator surface. This is used to then find a mapping between the plane and the scintillator.

Meanwhile, markers are also traced forward from the pinhole to the scintillator for each $\zeta = \zeta_1, \zeta_2, \ldots$ in an evenly spaced grid, in order to give us a spatial mapping between the pinhole and the scintillator. This is shown for two values of ζ in Fig. 6, with the mapping of the (R, Z) grid from the previous step overlaid onto the pinhole. Only the grid points that can pass from the pinhole onto the scintillator are shown; the other points correspond to markers that are blocked by the slits. For each value of ζ, the parts of the line from the previous step that overlap the grid of forward-passing points are found, and the result, shown in the pinhole as a set of green lines, shows the markers that can go both backward (to the virtual plane) and forward (to the scintillator). On the right, the

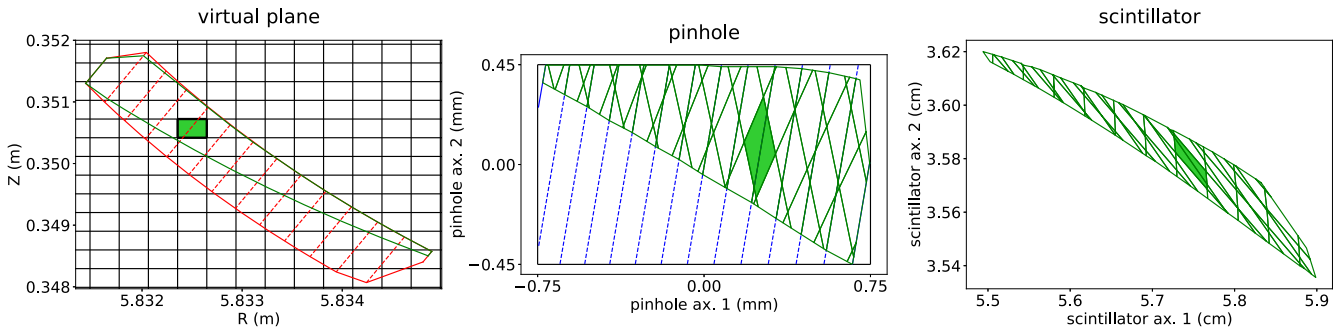

FIG. 7. By considering all possible values of ζ at the pinhole, a full mapping between the plane (left) and the scintillator (right) for markers with (χ, ρ_L, ζ') at the plane is determined. The green-outlined area in the leftmost plot denotes the area within which markers can travel to the scintillator and be measured, while the green shaded box corresponds to a specific (R, Z) bin at the plane which is then mapped to the pinhole (center) and from there to the scintillator. Each dashed line represents a specific value of ζ at the pinhole.

mapping of these green lines onto the scintillator is found using the grid points of where the forward-passing markers strike the scintillator.

Finally, combining these steps and looking at every possible value of ζ at the pinhole, we are able to find a mapping from the plane to the scintillator for markers at the plane with (χ, ρ_L, ζ'), as shown in Fig. 7. The red lines on the plane correspond to markers that can go from the plane to the pinhole and the green to markers that, once at the pinhole, can pass through onto the scintillator. For our chosen (R, Z) bin, outlined in bold on the plane and filled in with green, we can find its footprint on the scintillator. This bin is located entirely within the green polygon on the plane, meaning that all markers inside of it will reach the scintillator; its probability of transmission is thus 100%. For other (R, Z) bins, their probability is equal to the percentage of their area that overlaps with the area contained within the green lines. It can be seen that, using this method, the area in the corners of the pinhole is cut off. This is a result of performing simulations with a finite number of ζ values beginning at the pinhole. In future works, it may be possible to upgrade the analysis to extrapolate these areas, but in the meantime, the percentage of the overall area that is lost is not too large—for the example shown, with ζ steps at the pinhole of 0.025 rad, only 2.6% of the total pinhole area is lost.

To calculate the signal to the Faraday Cup (or, at least, the total flux of fast ions reaching the scintillator plate; it is not certain that all these ions will pass through the scintillator material into the Faraday Cup and be measured, although this is generally assumed[5]), only this probability is needed, and the mapping to the scintillator can be disregarded. As in Ref. 19, to find bins in (χ, ρ_L, ζ'), we average together all probabilities found for each value of each of these quantities within the desired bin size.

Then, for each marker passing through the plane, we sort it into a bin in $(R, Z, \chi, \rho_L, \zeta')$. We have the marker's weight, which corresponds to the total flux of fast ions per second it represents. We multiply this weight by the probability for this bin and then perform a boxcar sum over all markers, using the arrival time of each marker and the desired duration of the NBI, and multiply by the charge of each particle to get the signal as a current over time,

$$S(t) = \sum_i q_i w_i P(R_i, Z_i, \chi_i, \rho_{Li}, \zeta_i') \times (H(t - t_{i0}) - H(t - (t_{i0} + T_{NBI}))). \quad (6)$$

Here, i represents the marker, q_i its charge, w_i its weight, t_{i0} its arrival time, T_{NBI} is the duration of the NBI, and H is the Heaviside step function. The signal can be averaged over the expected sampling period of the digitizer; for this work, a 2 μs sampling time is assumed, the same as the NIFS-FILD digitizer.

In order to get the spatial distribution of the flux to the scintillator, the scintillator itself is divided into a grid. For each (R, Z) bin, such as the green shaded one shown in Fig. 7, we simply find the scintillator grid-boxes that it falls into and divide up the signal evenly among these boxes, as shown in Fig. 8. This is done rather than calculating the percentage of the green quadrilateral that falls into each separate grid box to save on computational time; for a small enough grid and a large enough number of $(R, Z, \chi, \rho_L, \zeta')$ sets, the differences should average out.

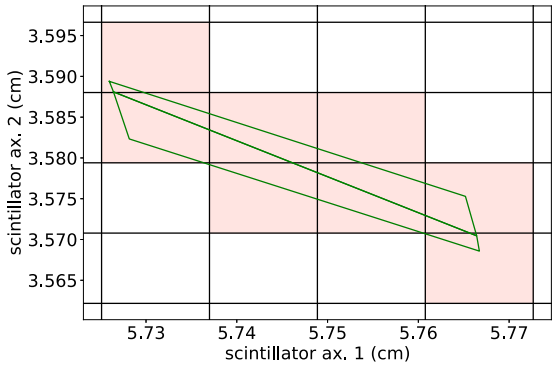

FIG. 8. Green quadrilateral, representing an (R, Z) bin mapped from the plane to the scintillator, is overlaid onto the scintillator grid and the boxes that it overlaps are found.

In this way, the probability for each (j, k) box on the scintillator, where j is the position along axis 1 and k is the position along axis 2, becomes

$$P_{j,k}(R, Z, \chi, \rho_L, \zeta') = \frac{P(R, Z, \chi, \rho_L, \zeta')}{N(R, Z, \chi, \rho_L, \zeta')_{boxes}}, \quad (7)$$

where $N(R, Z, \chi, \rho_L, \zeta')_{boxes}$ is the total number of boxes intersected, if this specific (j, k) box is one of the ones intersected and zero otherwise. For this work, a 120 × 120 grid was used for the area accessible to markers from each pinhole, although these grid boxes can be combined for the final calculation of the signal.

As with the total probability, once P has been separated into the grid on the scintillator, several points can be averaged together to get bins in (χ, ρ_L, ζ') Two separate grids are used for the two pinholes, as the areas of the scintillator accessible to them are far apart. The flux to each gridpoint on the scintillator can be calculated using Eq. (6), but replacing $P(R_i, Z_i, \chi_i, \rho_{Li}, \zeta_i')$ with $P_{i,j}(R_i, Z_i, \chi_i, \rho_{Li}, \zeta_i')$.

IV. RESULTS

For this work, the W7-X standard magnetic configuration was simulated using all the four commissioned neutral beam sources. These sources are numbered 3, 4, 7, and 8, where the former two are located within beam box NI20, within the lower half of the W7-X module 2, and the latter two are located within the beam box NI21, within the upper half of the same module. Sources 3 and 7 inject at a more radial angle to the magnetic axis, while sources 4 and 8 inject more tangentially. A neutralized power of 1.8 MW was assumed for all four sources, with 51%, 30%, and 19% of the power going to the full, half, and one-third energy beam components with 55, 27.5, and 18.3 keV, respectively. The temperature and density profiles used, which were chosen to match plausible W7-X operating conditions, were

$$n_e = 5e19 \times \left(\frac{3 - s^3}{3}\right) \mathrm{m}^{-3}, \quad (8)$$

$$T_e = 2 \times (1 - \sqrt{s}) \ \mathrm{keV}, \quad (9)$$

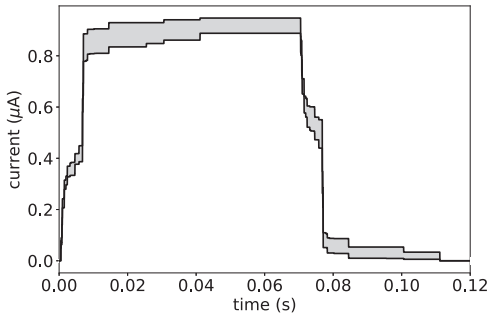

FIG. 9. Total simulated fast ion current reaching the scintillator plate of the S-FILD for a 70 ms injection of all four commissioned neutral beams in the W7-X standard magnetic configuration.

$$T_i = \min(T_e, 1.6)\ \text{keV}, \tag{10}$$

with $s = (r/a)^2$ being the flux surface label.

A. Simulated flux to Faraday Cup

First, the total flux of fast ions to the scintillator plate is calculated as a current, similar to Ref. 19, assuming an NBI duration of 70 ms for all four beam sources. The resulting current is shown in Fig. 9. This may not be the same as that measured by the Faraday Cup, as it is not certain that 100% of fast ions striking the plate will pass through the scintillator material and be captured by the Faraday Cup, although this has been assumed in past studies.[5] The band represents the uncertainty introduced by the choice of bin sizes in the analysis; the signal was calculated with several different bin sizes to find this uncertainty. Bin sizes used were $\delta\chi = 0.5°$, $\delta\rho_L = 0.05$ cm, $\delta\zeta' = \left[\frac{2\pi}{450}, \frac{2\pi}{300}, \frac{2\pi}{225}\right]$, $\delta R = [1.17, 1.46, 1.75]$ mm, and $\delta Z = [1.21, 1.52, 1.82]$ mm.

In Table I, the total percentage of the energy lost to collisions between the beam and the port, shinethrough, or losses out of the LCFS, along with the energy absorbed by the plasma and the contribution to the steady-state signal shown in Fig. 9 (averaged over the band of values) is shown for each of the four beam sources. It can be seen that total energy losses from the plasma alone do not determine the flux reaching the scintillator; this is because the ions arriving from each beam have different energies and pitch angles, and this is the primary determinant of their contribution to the signal.

TABLE I. Percent of total neutralized energy lost via different mechanisms or absorbed by the plasma for each neutral beam source, along with each beam's contribution to the steady-state ion current reaching the scintillator plate.

Beam	Port (%)	Shine. (%)	Lost (%)	Absorb. (%)	Signal (μA)
Source 3	7.6	19.0	26.9	46.6	0.30
Source 4	15.3	12.8	18.9	53.1	0.03
Source 7	7.97	18.8	17.6	55.6	0.20
Source 8	15.3	13.1	12.5	59.1	0.38

B. Spatial distribution of fast ion flux on the scintillator surface

Next, using the probability given by Eq. (7), the spatial distribution of the fast ion flux to the scintillator surface was simulated and is shown in Fig. 10. This simulates the proton impact density on the scintillator itself and is not the same thing as a synthetic camera signal; in order to simulate the signal seen by the camera, it would be necessary to also include the tilt and positioning of the scintillator with respect to the camera, the pixel size, the photon yield per ion of the TG-Green material, and the transmission efficiency of the optical system.

It can be seen that the entire contribution to the signal comes from the pinhole that measures the co-going fast ions. The pinhole measuring the counter-going ions sees no signal in these simulations—a result which differs from that found in Ref. 15. The reason for this is simple: although some fast ions produced by the NBI have higher pitch angles, the expanded markers arriving at the virtual plane for the counter-going pinhole have a maximum pitch angle of 101.6°, while the lowest pitch angle that has a non-zero probability of contributing to the signal is 105°. However, it is possible that the number of fast ions that would in reality arrive at this

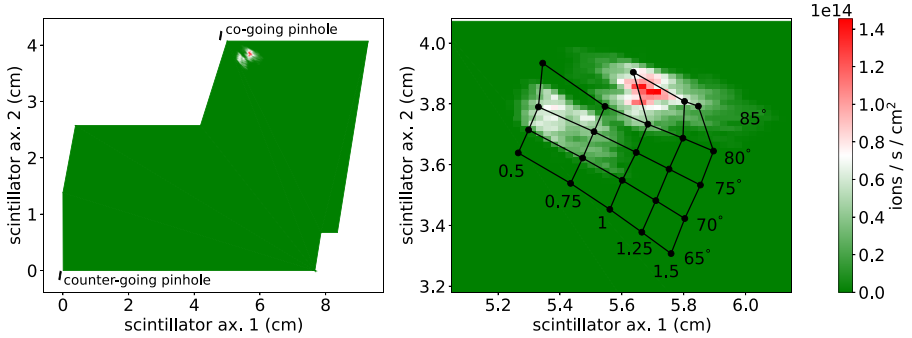

FIG. 10. Simulated steady-state flux of fast ions to the scintillator plate for all four neutral beams combined in the standard magnetic configuration. Only flux from co-going fast ions is observed.

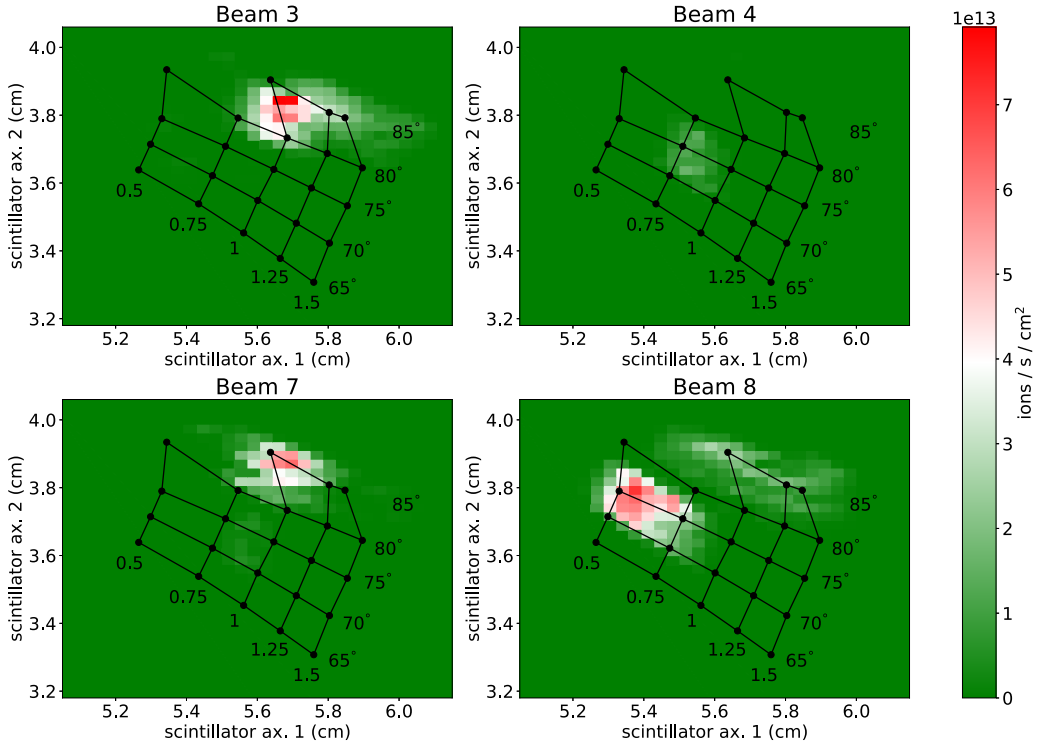

FIG. 11. Simulated steady-state flux of fast ions to the scintillator plate from each of the separate NBI sources included in the simulation.

virtual plane with a high enough pitch angle is simply below the resolution of the Monte Carlo simulations.

The results in Ref. 15 were found using a simpler method that took the gyroscalars and pitch angles of the markers reaching any part of the probe head and combined them with an "instrument function" produced by the FILDSIM code,[21,32] which gives the probability of arrival at the scintillator, as well as the location on the scintillator and rough spatial distribution of the signal, for markers with a specific gyroscalar and pitch angle, but with any gyrophase or location within the pinhole. While Ref. 15 also found the 105° limit, some of the markers that reached the probe head in the simulations performed in that work did have higher values of pitch angle than those reaching the virtual plane in this work.

In Fig. 11, the separate flux from each of the four beam sources is shown. It can be seen that ions from sources 3 and 7, which inject more radially, have higher pitch angles than from the more tangential beam sources 4 and 8. Ions arriving from sources 3 and 7 also have higher energies, although that is likely because high pitch-angle, low gyroscalar markers have a lower probability of making it through the pinhole. Finally, the contribution from source 4 is very small compared to the other three sources. Fewer markers from this beam arrive at the virtual plane, despite having similar levels of energy losses from the LCFS, suggesting that fast ions produced by this beam strike the wall at locations further from the S-FILD.

V. CONCLUSIONS

The first detailed simulation of fast ion fluxes into the probe head of the S-FILD, a new diagnostic designed for steady-state operation in W7-X, has revealed several key findings.

It can be seen that the total flux of fast ions to the detector is comparable with that seen by the NIFS-FILD already implemented in W7-X[10] and should be measurable with this diagnostic. In addition, we observe a low signal from one of the four commissioned neutral beam sources, suggesting that the other three sources should likely be preferentially used for experiments making use of the S-FILD.

Finally, no flux of counter-going ions is seen. Once the S-FILD is implemented into the machine, measurements taken with this magnetic field configuration and similar densities and temperatures can determine the merits of this detailed approach to simulation: if no counter-going ions are measured, it would suggest that the method defined in this work is more accurate, while if they are measured, the method detailed in Ref. 15 may be more appropriate. In addition, it may be worthwhile to use this method to simulate other magnetic field configurations and insertion depths of the S-FILD. Comparisons between experimental measurements and the simulations presented in this paper will validate our understanding of fast ion losses in optimized stellarators and help enable predictions of fast ion confinement in future stellarators.

ACKNOWLEDGMENTS

This work was supported by the U.S. Department of Energy under Contract No. DE-AC02-09CH11466. This work has been carried out within the framework of the EUROfusion Consortium, funded by the European Union via the Euratom Research and Training Programme (Grant Agreement No. 101052200—EUROfusion). Views and opinions expressed are, however, those of the author(s) only and do not necessarily reflect those of the European Union or the European Commission. Neither the European Union nor the European Commission can be held responsible for them.

Simulations for this work were performed at the Max Planck Computing and Data Facility on the systems Cobra and Raven. The authors thank the members of the ASCOT group based at Aalto University (Finland) for allowing use of their code ASCOT5 and for their support of this work. BEAMS3D runs were performed with v3.50 of the code, "develop" branch, hash 4d1344e90b78272bd6d9b5c4453fd352d12611eb. ASCOT5 runs were performed with v5.3 of the code, "master" branch, hash bb5742377bc6a4919aeba3ffeda05e41a4e8f1c6.

AUTHOR DECLARATIONS

Conflict of Interest

The authors have no conflicts to disclose.

Author Contributions

A. LeViness: Conceptualization (lead); Formal analysis (lead); Investigation (lead); Methodology (lead); Writing – original draft (lead). **S. A. Lazerson**: Conceptualization (equal); Software (lead); Supervision (equal); Writing – review & editing (equal). **A. Jansen van Vuuren**: Conceptualization (equal); Formal analysis (equal); Investigation (equal). **J. Rueda-Rueda**: Methodology (supporting); Software (equal). **J. Ayllon-Guerola**: Formal analysis (equal). **S. Bozhenkov**: Investigation (equal). **D. Corl**: Conceptualization (equal); Formal analysis (equal). **R. Ellis**: Conceptualization (equal); Formal analysis (equal). **J. Galdon-Quiroga**: Formal analysis (equal). **J. Garcia-Dominguez**: Conceptualization (equal); Formal analysis (equal). **M. Garcia-Munoz**: Conceptualization (equal); Resources (equal). **J. Hidalgo-Salaverri**: Formal analysis (equal). **K. Ogawa**: Investigation (supporting). **N. Pablant**: Funding acquisition (equal); Supervision (equal); Writing – review & editing (equal). **J. Segado-Fernandez**: Formal analysis (equal).

DATA AVAILABILITY

The data that support the findings of this study are available from the corresponding author upon reasonable request.

REFERENCES

[1]D. A. Gates *et al.*, "Stellarator research opportunities: A report of the national stellarator coordinating committee," J. Fusion Energy **37**, 51 (2018).
[2]W. Lotz, P. Merkel, J. Nührenberg, and E. Strumberger, "Collisionless alpha-particle confinement in stellarators," Plasma Phys. Controlled Fusion **34**, 1037 (1992).
[3]D. S. Darrow, H. W. Herrmann, D. W. Johnson, R. J. Marsala, R. W. Palladino, S. J. Zwebens, and M. Tuszewski, "Measurement of loss of DT fusion products using scintillator detectors in TFTR (invited)," Rev. Sci. Instrum. **66**, 476 (1995).
[4]M. Isobe *et al.*, "Escaping fast ion diagnostics in compact helical system heliotron/torsatron," Rev. Sci. Instrum. **70**, 827 (1999).
[5]D. S. Darrow, R. Bell, D. W. Johnson, H. Kugel, J. R. Wilson, F. E. Cecil, R. Maingi, A. Krasilnikov, and A. Alekseyev, "Fast ion loss diagnostic plans for the national spherical torus experiment," Rev. Sci. Instrum. **72**, 784–787 (2001).
[6]M. García-Muñoz, H.-U. Fahrbach, H. Zohm, and ASDEX Upgrade Team, "Scintillator based detector for fast-ion losses induced by magnetohydrodynamic instabilities in the ASDEX upgrade tokamak," Rev. Sci. Instrum. **80**, 053503 (2009).
[7]M. García-Muñoz *et al.*, "Conceptual design of the ITER fast-ion loss detector," Rev. Sci. Instrum. **87**, 11D829 (2016).
[8]J. F. Chang *et al.*, "Scintillator-based fast ion loss measurements in the EAST," Rev. Sci. Instrum. **87**, 11E728 (2016).
[9]D. Nicolai *et al.*, "A multi-purpose manipulator system for W7-X as user facility for plasma edge investigation," Fusion Eng. Des. **123**, 960 (2017).
[10]K. Ogawa *et al.*, "Energy-and-pitch-angle-resolved escaping beam ion measurements by Faraday-cup-based fast-ion loss detector in Wendelstein 7-X," J. Inst. **14**, C09021 (2019).
[11]S. A. Lazerson, R. Ellis, C. Freeman, J. Ilagan, T. Wang, L. Shao, N. Allen, D. Gates, and H. Neilson, "Development of a Faraday cup fast ion loss detector for keV beam ions," Rev. Sci. Instrum. **90**, 093504 (2019).
[12]D. Kulla, S. A. Lazerson, K. Hunger, H. Gerdes, and R. Bandorf, "Layer thickness characterization of Faraday cup fast ion loss detectors," Rev. Sci. Instrum. **94**, 053503 (2023).
[13]S. A. Lazerson, D. Kulla, A. LeViness, B. Lee, M. Steffan, B. Kursinski, and K. Ewert, "First measurements of escaping energetic ions by the Faraday cup fast ion loss detector on Wendelstein 7-X" (submitted) (2024).
[14]A. Jansen van Vuuren *et al.*, "Conceptual design of a scintillator-based fast-ion loss detector for the Wendelstein 7-X stellarator," IEEE Trans. Plasma Sci. **50**, 4114 (2022).
[15]A. Jansen van Vuuren *et al.*, "Development of a scintillator based fast-ion loss detector for the Wendelstein 7-X stellarator," Fusion Eng. Des. **204**, 114520 (2024).
[16]A. Werner, A. Weller, D. S. Darrow, and W7-AS Team, "Fast ion losses in the W7-AS stellarator," Rev. Sci. Instrum. **72**, 780 (2001).
[17]D. S. Darrow, "Scintillator based energetic ion loss diagnostic for the national spherical torus experiment," Rev. Sci. Instrum. **79**, 023502 (2008).
[18]J. Kim, J. Y. Kim, S. W. Yoon, M. García-Muñoz, M. Isobe, and W. C. Kim, "Initial measurements of fast ion loss in KSTAR," Rev. Sci. Instrum. **83**, 10D305 (2012).
[19]A. LeViness *et al.*, "Validation of a synthetic fast ion loss detector model for Wendelstein 7-X" (submitted) (2024).
[20]B. S. Schmidt *et al.*, "Anisotropic regularization for inversion of fast-ion loss detector measurements" (submitted) (2024).
[21]J. Galdón-Quiroga *et al.*, "Velocity-space sensitivity and tomography of scintillator-based fast-ion loss detectors," Plasma Phys. Controlled Fusion **60**, 105005 (2018).
[22]M. Rodríguez-Ramos, M. Jiménez-Ramos, M. García-Muñoz, and J. García-López, "Temperature response of several scintillator materials to light ions," Nucl. Instrum. Methods Phys. Res., Sect. B **403**, 7–12 (2017).
[23]S. Håkan, NEOTRANSP, 2021, https://gitlab.mpcdf.mpg.de/smithh/neotransp.
[24]W. I. van Rij and S. P. Hirshman, "Variational bounds for transport coefficients in three-dimensional toroidal plasmas," Phys. Fluids B **1**, 563–569 (1989).
[25]S. A. Lazerson *et al.*, "Validation of the BEAMS3D neutral beam deposition model on Wendelstein 7-X," Nucl. Fusion **60**, 076020 (2020).
[26]M. McMillan and S. A. Lazerson, "BEAMS3D neutral beam injection model," Plasma Phys. Controlled Fusion **56**, 095019 (2014).
[27]S. A. Lazerson *et al.*, "First neutral beam experiments on Wendelstein 7-X," Nucl. Fusion **61**, 096008 (2021).

[28]S. A. Lazerson *et al.*, "Neutral beam experiments with upgraded power on Wendelstein 7-X," in 29th IAEA Fusion Energy Conference (FEC 2023), 2023.
[29]S. A. Lazerson *et al.*, "Modeling and measurement of energetic particle slowing down in Wendelstein 7-X," Nucl. Fusion **61**, 096005 (2021).
[30]J. Varje, K. Särkimäki, J. Kontula, P. Ollus, T. Kurki-Suonio, A. Snicker, E. Hirvijoki, and S. Äkäslompolo, "High-performance orbit-following code ASCOT5 for Monte Carlo simulations in fusion plasmas," arXiv:1908.02482 (2019).
[31]D. Kulla, S. A. Lazerson, S. Günter, M. Hirsch, D. Hartmann, P. McNeely, N. Rust, and R. C. Wolf, "Placement of a fast ion loss detector array for neutral beam injected particles in Wendelstein 7-X," Plasma Phys. Controlled Fusion **64**, 035006 (2022).
[32]B. S. Schmidt *et al.*, "A new FILDSIM model for improved velocity-space sensitivity modelling and reconstructions," Plasma Phys. Controlled Fusion **66**, 045004 (2024).